CHALMERS
UNIVERSITY OF TECHNOLOGY

Opposite effects of flame-generated potential and solenoidal velocity fluctuations on flame surface area in moderately intense turbulence

Proceedings of the Combustion Institute 40 (2024) 105238

Contents lists available at ScienceDirect

Proceedings of the Combustion Institute

journal homepage: www.elsevier.com/locate/proci

Opposite effects of flame-generated potential and solenoidal velocity fluctuations on flame surface area in moderately intense turbulence

Andrei N. Lipatnikov [a,*], Vladimir A. Sabelnikov [b,c], Nikolay V. Nikitin [d]

[a] Department of Mechanics and Maritime Sciences, Chalmers University of Technology, Göteborg, 412 96, Sweden
[b] ONERA - The French Aerospace Lab., F-91761 Palaiseau, France
[c] Central Aerohydrodynamic Institute (TsAGI), 140180 Zhukovsky, Moscow Region, Russian Federation
[d] Institute of Mechanics, Lomonosov Moscow State University, 119991, Moscow, Russian Federation

ARTICLE INFO

Keywords:
Flame speed
Burning velocity
Flame surface area
Vorticity
Strain rate
Helmholtz–Hodge decomposition

ABSTRACT

To explore the influence of dilatational and rotational motions on iso-scalar surface area within a premixed turbulent flame, three-dimensional compressible direct numerical simulation data obtained by Dave et al. (2018) from a lean, complex-chemistry, hydrogen-air flame propagating in intense small-scale turbulence (a ratio of laminar flame thickness to Kolmogorov length scale is about 20) in a box are analyzed using Helmholtz–Hodge decomposition of velocity field into solenoidal and potential components. The obtained results indicate that the flame surface area is created by potential velocity fluctuations generated due to combustion-induced thermal expansion, whereas the rotational motion acts to smooth wrinkles of iso-scalar surfaces within local preheat and reaction zones and, consequently, to reduce the flame surface area. The latter finding challenges the classical concept of flame-generated turbulence and is attributed to flame-generated solenoidal velocity fluctuations. Specifically, the incoming tangential (to the flame) vorticity is suppressed by baroclinic torque, which also generates vorticity in another tangential direction, with the latter (flame-generated) solenoidal velocity fluctuations working to smooth the flame surface. Thus, even under conditions of moderately intense turbulence, flame surface area can primarily be created by potential velocity perturbations caused by combustion-induced thermal expansion.

1. Introduction

Since turbulence in a typical laboratory burner is primarily rotational motion, an increase in premixed burning rate by turbulence is often attributed to the influence of vortices on a flame. In particular, such a view motivated numerous computational and experimental studies of flame-vortex interaction, e.g., see a review article by Renard et al. [1] and recent papers by Thiesset et al. [2], Paes et al. [3], or Luna and Egolfopoulos [4]. Within the framework of such a paradigm, flame-generated vorticity is often believed to accelerate premixed combustion. Nevertheless, there are theoretical, experimental, and numerical data that indicate the opposite effect. First, Darrieus–Landau theory of hydrodynamic instability of an infinitely thin laminar premixed flame [5,6] predicts that rotational and potential velocities generated by the instability have opposite directions just downstream of the flame sheet, with the rotational motion pushing the sheet perturbations back, see Eq. (40) in a review article by Lipatnikov and Chomiak [7]. Second, (i) experimental studies [8,9] of the interaction of a large laminar toroidal vortex with a relatively thin premixed flame and (ii) two-dimensional (2D) numerical simulations [10–12] of the interaction of a laminar vortex pair (a 2D approximation of a toroidal vortex) with a laminar premixed flame have shown that vorticity signs may be opposite upstream and downstream of the flame, i.e., vorticity generated by baroclinic torque $\nabla\rho\times\nabla p$ in the flame can stabilize perturbations of the flame surface, caused by the incoming vortices. Here, ρ and p are the density and pressure, respectively. A similar effect was documented in experiments with three weakly turbulent Bunsen flames [13]. Finally, a recent analysis [14,15] of three-dimensional (3D) Direct Numerical Simulation (DNS) data obtained from two weakly turbulent single-step-chemistry flames has shown that the local flame stretch rate is predominantly negative in regions characterized by a large magnitude of baroclinic torque or a large magnitude of enstrophy. Thus, strong flame-generated vorticity impeded wrinkling reaction zones under conditions of that study.

While such a phenomenon is of fundamental interest for understanding the physics of premixed turbulent combustion (in particular, flame-generated turbulence and its effect on burning rate), it has not yet attracted due attention. This lack of due attention stems, probably, from

* Corresponding author.
E-mail address: lipatn@chalmers.se (A.N. Lipatnikov).

https://doi.org/10.1016/j.proci.2024.105238
Received 4 December 2023; Accepted 22 May 2024
Available online 24 June 2024

the facts that a few earlier studies either (i) used 2D optical diagnostic or numerical tools [8–12] or/and (ii) dealt with laminar [5,6,8–12] or weakly-turbulent [13–15] flames. While the influence of combustion-induced thermal expansion on certain turbulence characteristics was shown to be weak in very intense turbulence, as reviewed elsewhere [7, 16,17], the present authors are not aware on research into effects of flame-generated potential and solenoidal velocity fluctuations on iso-scalar surface areas within a premixed flame under conditions of moderately intense, small-scale turbulence.

In addition, all the aforementioned simulations [10–12,14,15] dealt with single-step combustion chemistry. While the present authors are not aware on an argument that implies a substantial influence of combustion chemistry on vorticity evolution within a premixed flame, the lack of such an influence should nevertheless be demonstrated.

Accordingly, the present paper aims at bridging this knowledge gap by reporting DNS data, which show, for the first time to the authors' knowledge, that, under conditions of moderately intense, small-scale turbulence, (i) flame-generated solenoidal velocity fluctuations statistically smooth 3D wrinkles on flame surface, (ii) which, nevertheless, grow due to potential velocity fluctuations generated due to combustion-induced thermal expansion.

2. Numerical simulations

2.1. DNS attributes

The DNS data analyzed here were computed by Dave et al. [18,19] and were also explored in other recent papers [20–25]. The data were obtained from an unconfined, statistically one-dimensional and planar, lean (the equivalence ratio $\phi = 0.81$), and slightly preheated (unburned gas temperature $T_u = 310$ K) H_2-air flame propagating in a box ($19.18 \times 4.8 \times 4.8$ mm) meshed using a uniform grid of $960 \times 240 \times 240$ cells. The mixture-averaged transport model and a "comprehensive kinetic model" by Li et al. [26] (21 reactions, 9 species) were adopted. The laminar flame speed $S_L = 1.84$ m/s, thickness $\delta_L = (T_b - T_u)/\max\{|\nabla T|\} = 0.36$ mm, and time scale $\tau_f = \delta_L/S_L = 0.20$ ms, where subscripts u and b designate unburned and burned gases, respectively.

Homogeneous isotropic turbulence was pre-generated using forcing at low wavenumbers in a separate cube with the fully periodic boundary conditions. The generation process was performed until a statistically stationary stage was reached. The obtained turbulence displays the Kolmogorov–Obukhov 5/3 spectrum [5] and is characterized by the r.m.s. velocity $u' = 6.7$ m/s, an integral length scale $L = 3.1$ mm, the turbulent Reynolds number $Re_t = u'L/\nu_u = 950$, the Kolmogorov length scale $\eta_K = (\nu_u^3/\langle\varepsilon\rangle)^{1/4} = 0.018$ mm, the integral and Kolmogorov time scales $\tau_t = L/u' = 0.46$ ms and $\tau_K = (\nu_u/\langle\varepsilon\rangle)^{1/2} = 0.015$ ms, respectively. Here, $\langle\varepsilon\rangle = 2\nu_u\langle S_{ij}S_{ij}\rangle$ designates the rate of dissipation of turbulent kinetic energy, averaged over the cube; ν is kinematic viscosity; $S_{ij} = 0.5(\partial u_i/\partial x_j + \partial u_j/\partial x_i)$ is the rate-of-strain tensor; and the Einstein summation convention applies to repeated indexes. Accordingly, the Damköhler number $Da = \tau_t/\tau_f = 2.35$ and the number $(\delta_L/\eta_K)^2$, which is sometimes associated with Karlovitz number, is as large as 400. Note, that a more appropriate Karlovitz number $Ka = \tau_f/\tau_K = 13$ is significantly less, because $S_L\delta_L/\nu_u \gg 1$ in lean H_2-air flames [27].

When running combustion simulations, the pre-generated turbulence was continuously injected into the computational domain through the left boundary and decayed along the mean flow direction x (symmetry boundary conditions were set at transverse boundaries). Accordingly, $u' = 3.3$ m/s and $Ka = 3.3$ at the leading edge of the mean flame brush, associated with the transverse-averaged value $\bar{c}_F(x,t)$ of the fuel-based combustion progress variable equal to 0.01. Nevertheless, the turbulence length scales evaluated at the inlet boundary and at the leading edge are roughly equal to one another, i.e., $(\delta_L/\eta_K)^2$ is still about 400 at the leading edge. Here, $c_F = (Y_F - Y_{F,u})/(Y_{F,b} - Y_{F,u})$ is defined using the fuel mass fraction Y_F to satisfy a constraint of $0 \le c_F \le 1$, whereas local values of temperature-based combustion progress variable can be larger than unity due to differences in molecular diffusivities of heat, H_2, and O_2 [28,29].

2.2. Velocity decomposition

The computed turbulent velocity field $\mathbf{u}(\mathbf{x},t)$ was decomposed into potential and solenoidal components, $\mathbf{u}_p(\mathbf{x},t)$ and $\mathbf{u}_s(\mathbf{x},t)$, respectively, using a numerical method applied earlier by the present authors to two weakly turbulent single-step chemistry flames [30] and two other complex-chemistry flames [31–33]. This method yields

$$\mathbf{u}(\mathbf{x},t) = \mathbf{u}_p(\mathbf{x},t) + \mathbf{u}_s(\mathbf{x},t);$$
$$\nabla \times \mathbf{u}_p(\mathbf{x},t) = 0; \qquad \nabla \cdot \mathbf{u}_s(\mathbf{x},t) = 0. \tag{1}$$

The key difference between solenoidal and potential velocity fields consists of the fact that the former is dilatation-free, i.e., combustion-induced dilatation directly affects the potential velocity field only.

2.3. Conditioned quantities

Quantities conditioned to the instantaneous local values $c_F(\mathbf{x},t)$ of the combustion progress variable, reported in the following, were sampled from volumes characterized by $0.005 \le c_F(\mathbf{x},t) < 0.995$ by dividing an interval of a sampling variable $\xi \in [0.005, 0.995)$ in 100 bins, e.g., $\langle\mathbf{u}_s|\xi\rangle$ designates the solenoidal velocity vector sampled from and averaged over volumes characterized by $\xi - 0.005 \le c_F(\mathbf{x},t) < \xi + 0.005$. Results sampled at $c_F(\mathbf{x},t) < 0.005$ and $c_F(\mathbf{x},t) \ge 0.995$ are disregarded, because (i) the focus of this study is placed on velocity fluctuations within flames, but (ii) statistics sampled from these two bins are mainly controlled by velocity fluctuations in fresh reactants and burned products, respectively. The sampling was applied either to the entire computational domain or to a band of $c_i^* - 0.01 < \bar{c}_F(x,t) < c_i^* + 0.01$, where $c_i^* = 0.1$, 0.3, 0.5, 0.7, or 0.9. In the following, dependencies of conditioned quantities on the local combustion progress variable c_F or the mean combustion progress variable $\bar{c}_F$ will be referred to as variations of these quantities in flame or flame brush, respectively, i.e., word "flame" will designate instantaneous local flame. Moreover, since $\langle q|\xi\rangle \equiv \langle q|\xi - 0.005 \le c_F(\mathbf{x},t) < \xi + 0.005\rangle$ for any quantity q, the former variations will be discussed in terms of ξ-dependence of the conditioned $\langle q|\xi\rangle$.

Conditioned quantities reported in the following were sampled from 56 snapshots stored each 5 μs over $2.8 \le t/\tau_t \le 3.4$ and time-averaged. During this time interval, statistical stationarity of the flame propagation was reached, e.g., turbulent burning velocity oscillated weakly around a steady value [20].

3. Results and discussion

3.1. Potential and solenoidal mass fluxes

Figs. 1a and 1b show dimensionless conditioned normal mass fluxes $m_{n,s} \equiv \langle\mathbf{n}\cdot\rho\mathbf{u}_s|\xi\rangle/(\rho_u S_L)$ and $m_{n,p} \equiv \langle\mathbf{n}\cdot\rho\mathbf{u}_p|\xi\rangle/(\rho_u S_L)$, sampled from different zones of the mean flame brush. Since the normal unit vector $\mathbf{n} = -\nabla c_F/|\nabla c_F|$ points to unburned reactants, the normal mass fluxes are negative when the corresponding velocities convect the flame to combustion products. The following trends are worth emphasizing.

First, the magnitude of the solenoidal normal flux $m_{n,s}$ is less than the magnitude of the potential normal flux $m_{n,p}$, thus, indicating that convection of flames in direction normal to them is mainly controlled by the potential motion.

Second, the magnitude of the potential $m_{n,p}$, which is negative, i.e., $\mathbf{u}_p$ convects the flame to products, decreases with increasing ξ, with the exception of the flame-brush zone characterized by $\bar{c}_F \approx 0.1$, see Fig. 1b. Since such a behavior of the normal mass flow rate is known for strained laminar flames [6,34], the discussed trend could be attributed to generation of predominantly positive strain rates by the potential velocity field, as will be discussed later.

Third, the solenoidal flux signs are opposite at $\bar{c}_F = 0.1$ or 0.3 and $\bar{c}_F = 0.7$ or 0.9. More specifically, the solenoidal velocity predominantly

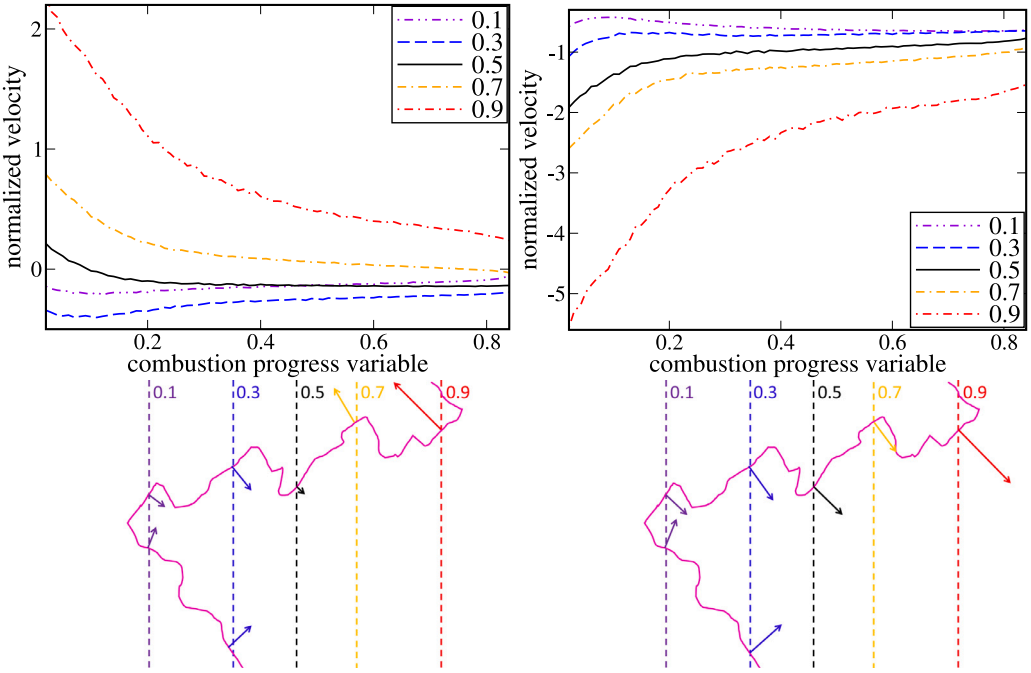

Fig. 1. Dependencies of dimensionless conditioned (*a*) solenoidal $\langle \mathbf{n}\cdot\rho\mathbf{u}_s|\xi\rangle/(\rho_u S_L)$ and (*b*) potential $\langle \mathbf{n}\cdot\rho\mathbf{u}_p|\xi\rangle/(\rho_u S_L)$ normal mass fluxes on ξ, sampled from different bands $c_i^* - 0.01 < \bar{c}_F(x,t) < c_i^* + 0.01$, with c_i^* being specified in legends. Sketches of the influence of (*c*) solenoidal and (*d*) potential velocities on an instantaneous local flame surface (solid magenta line). Vertical straight dashed lines show mean surfaces $\bar{c}_F(x,t) = c_i^*$, with c_i^* being specified near the lines. (For interpretation of the references to color in this figure legend, the reader is referred to the web version of this article.)

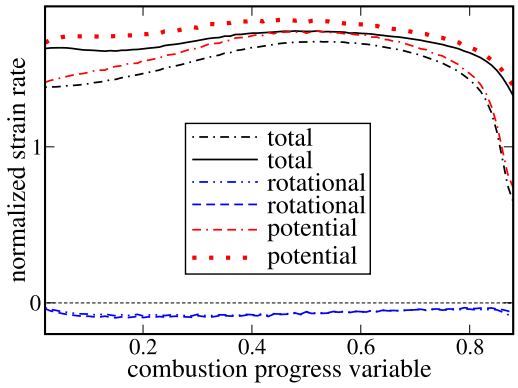

Fig. 2. Normalized conditioned strain rates (black lines) sampled from the entire computational domain, as well as potential (red lines) and solenoidal (blue lines) contributions to them. $\tau_f\langle a_t|\xi\rangle$ are plotted in dotted-dashed lines. Other curves show $\tau_f\langle a_t|\nabla c_F||\xi\rangle/\langle|\nabla c_F||\xi\rangle$. (For interpretation of the references to color in this figure legend, the reader is referred to the web version of this article.)

convects flames to (from) products in the leading (trailing, respectively) halves of the flame brush. This is illustrated in Fig. 1c, where arrows show direction of $m_{n,s}$, the arrow length characterizes $|m_{n,s}|$, and vertical dashed lines represent mean surfaces of $\bar{c}_F(x,t) = c_i^*$, with c_i^* being specified near the lines. The emphasized changes in $m_{n,s}$ with $\bar{c}_F$ imply that the solenoidal velocity predominantly convects flames to the middle of the flame brush both from its leading and trailing halves, thus, damping perturbations of the axial coordinate x_f of the flame surface. Accordingly, the solenoidal velocity field works to decrease the flame surface area. On the contrary, the potential $m_{n,p}$ points to products at various $\bar{c}_F$ and $|m_{n,p}|$ is increased with increasing $\bar{c}_F$.

3.2. Potential and solenoidal strain rates

To support the above interpretation of Fig. 1, let us compare contributions of potential and solenoidal velocity fields to the flame strain rate $a_t = \nabla\cdot\mathbf{u} - \mathbf{n}\cdot\nabla\mathbf{u}\cdot\mathbf{n}$. The point is that the time derivative of the area A_f of an infinitesimal element of an iso-scalar surface $c_F(\mathbf{x},t) = \xi$ is known to be controlled by the local flame stretch rate $\dot{s}$ [35–38], i.e.,

$$\frac{1}{A_f}\frac{\mathrm{d}A_f}{\mathrm{d}t} = \dot{s} = a_t + S_d\nabla\cdot\mathbf{n}. \tag{2}$$

In particular, a transport equation for flame surface density [38–40], i.e., flame surface area per unit volume, involves both the strain rate a_t and the curvature term $S_d\nabla\cdot\mathbf{n}$. Here, $\nabla\cdot\mathbf{n}$ characterizes the local flame curvature and, for any iso-scalar surface, the flame displacement speed S_d is evaluated as follows $S_d = |\nabla c_F|^{-1}\left(\partial c_F/\partial t + \mathbf{u}\cdot\nabla c_F\right)$.

While separation of contributions of potential and solenoidal velocity fields to the curvature term $S_d\nabla\cdot\mathbf{n}$ is difficult, such a separation is of minor interest for the goals of the present study, because this curvature term is predominantly negative in various premixed turbulent flames [41–46], i.e., this term works statistically to reduce flame surface density. On the contrary, the mean strain rate is positive in those flames [41–46], i.e., flame surface is predominantly created by turbulent strain rates. Since the strain rate a_t is linear with respect to the velocity vector $\mathbf{u}$, contributions of potential and solenoidal velocity fields to a_t can easily be separated. Accordingly, comparison of conditioned values of $a_{t,p} = \nabla\cdot\mathbf{u}_p - \mathbf{n}\cdot\nabla\mathbf{u}_p\cdot\mathbf{n}$ and $a_{t,s} = -\mathbf{n}\cdot\nabla\mathbf{u}_s\cdot\mathbf{n}$ offers the opportunity to explore the effects of potential and solenoidal velocity fields on flame surface area generation.

Total (black solid line), potential (red dotted line), and solenoidal (blue dashed line) conditioned strain rates $\langle a_t|\xi\rangle$ are compared in Fig. 2. Since similar results were obtained from various flame-brush zones, only results sampled from the entire flame brush are reported. Note that the differently conditioned strain rates $\langle a_t\rangle_\xi \equiv \langle a_t|\nabla c_F||\xi\rangle/\langle|\nabla c_F||\xi\rangle$, which are associated with the transport equation for $\overline{|\nabla c_F|}$ [40], evolve similarly to $\langle a_t|\xi\rangle$, cf. a dotted-dashed line with another line of the same color.

Fig. 2 shows that, first, the mean strain rates, i.e., $\overline{a_t}$, $\overline{a_{t,p}}$, and $\overline{a_{t,s}}$ plotted in dotted-dashed lines, and the flame-conditioned strain rates $\langle a_t\rangle_\xi$, $\langle a_{t,p}\rangle_\xi$, and $\langle a_{t,s}\rangle_\xi$, respectively, plotted in solid, dotted, and dashed lines, respectively, are close to one another, i.e., $\overline{a_t} \approx \langle a_t\rangle_\xi$,

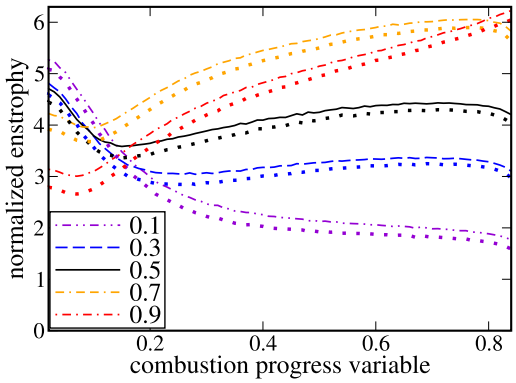

Fig. 3. Dependencies of normalized conditioned magnitude of tangential vorticity $\tau_f\langle\sqrt{(\boldsymbol{\omega}-(\mathbf{n}\cdot\boldsymbol{\omega})\mathbf{n})^2}|\xi\rangle$ (dotted lines) and enstrophy $\tau_f\langle\sqrt{\omega^2}|\xi\rangle$ (other lines) on ξ, sampled from bands of $c_i^*-0.01<\bar{c}_F(x,t)<c_i^*+0.01$, with c_i^* being specified in legends.

$\overline{a_{t,p}} \approx \langle a_{t,p}\rangle_\xi$, and $\overline{a_{t,s}} \approx \langle a_{t,s}\rangle_\xi$ under conditions of the present study. Second, the total strain rate $\overline{a_t}$ ($\langle a_t\rangle_\xi$) or the potential strain rate $\overline{a_{t,p}}$ ($\langle a_{t,p}\rangle_\xi$) is significantly larger than the magnitude $|\overline{a_{t,s}}|$ ($|\langle a_{t,s}\rangle_\xi|$) of the solenoidal strain rate. Third, the total strain rates $\overline{a_t}$ and $\langle a_t\rangle_\xi$ or the potential strain rates $\overline{a_{t,p}}$ and $\langle a_{t,p}\rangle_\xi$ are positive, whereas the solenoidal strain rates $\overline{a_{t,s}}$ and $\langle a_{t,s}\rangle/_\xi$ are negative. Thus, under conditions of the present study, strain rates created by the potential velocity field work predominantly to increase flame surface area, whereas strain rates created by the solenoidal velocity field work statistically to reduce the area, in line with discussion of Fig. 1. Consistency of results shown in Figs. 1 and 2 validates the present analysis, because the results have been obtained using different numerical diagnostic tools.

3.3. Vorticity rotation in flames

Since the incoming vorticity is widely accepted to wrinkle flame surface and increase its area in a turbulent flow, the DNS data shown in Figs. 1 and 2 imply that thermal expansion results in generating counter-rotating (with respect to the incoming flow) vorticity, with strain rates created by the corresponding solenoidal velocity fluctuations statistically smoothing flame surface. The following discussion aims at supporting this interpretation of the DNS data.

Fig. 3 shows that, within flames, the conditioned enstrophy $\langle\sqrt{\omega^2}|\xi\rangle$ decreases with increasing ξ at low $c_F(\mathbf{x},t)$, i.e., on the flame unburned side, with the effect being most pronounced at low $\bar{c}_F$, i.e., at the flame-brush leading edge. Here, $\omega^2=\boldsymbol{\omega}\cdot\boldsymbol{\omega}$ and $\boldsymbol{\omega}=\nabla\times\mathbf{u}$ is vorticity vector. At larger $c_F(\mathbf{x},t)$, dependencies of $\langle\sqrt{\omega^2}|\xi\rangle$ on ξ are weak if $\bar{c}_F\le 0.5$, but $\langle\sqrt{\omega^2}|\xi\rangle$ is increased with ξ at $\bar{c}_F>0.5$ and $\xi>0.1$. Besides, comparison of curves plotted in dotted lines with other curves in Fig. 3 shows that contribution of the normal (to the flame) component of the vorticity vector $\boldsymbol{\omega}$ to enstrophy is much less than contribution of the tangential vorticity $\boldsymbol{\omega}_t=\boldsymbol{\omega}-(\mathbf{n}\cdot\boldsymbol{\omega})\mathbf{n}$. In other words, the vectors $\boldsymbol{\omega}$ and $\mathbf{n}$ misalign, in line with earlier DNS studies of turbulent mixing [47] and highly turbulent premixed flames [48].

To further explore the above trends, let us consider the following well-known enstrophy transport equation [7,17,49]

$$\frac{1}{2}\frac{\partial\omega^2}{\partial t}+\frac{1}{2}u_k\frac{\partial\omega^2}{\partial x_k}=\underbrace{\omega_i\omega_k\frac{\partial u_i}{\partial x_k}}_{T_1}\underbrace{-\omega^2\frac{\partial u_k}{\partial x_k}}_{T_2}$$
$$+\underbrace{\varepsilon_{ijk}\omega_i\frac{1}{\rho^2}\frac{\partial\rho}{\partial x_j}\frac{\partial p}{\partial x_k}}_{T_3}+\underbrace{\varepsilon_{ijk}\omega_i\frac{\partial}{\partial x_l}\left(\frac{1}{\rho}\frac{\partial\tau_{kl}}{\partial x_j}\right)}_{T_4} \quad (3)$$

where ω_i is a component of the vorticity vector $\boldsymbol{\omega}$,

$$\tau_{kl}=\rho\nu\left(\frac{\partial u_k}{\partial x_l}+\frac{\partial u_l}{\partial x_k}-\frac{2}{3}\delta_{kl}\frac{\partial u_k}{\partial x_l}\right)$$

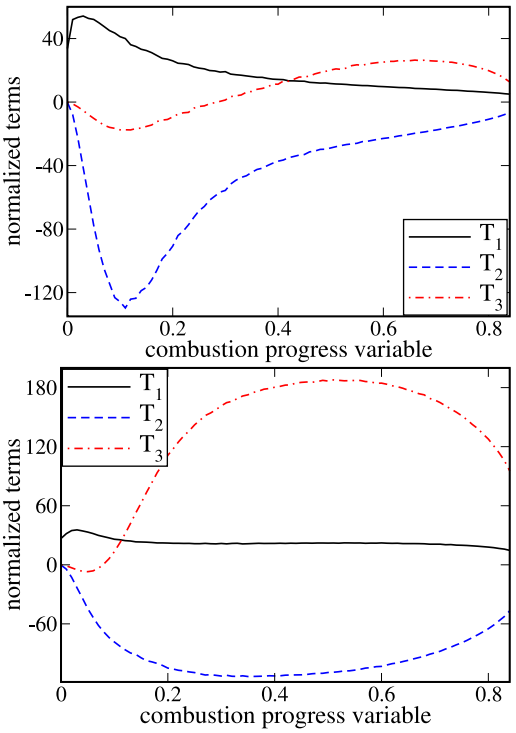

Fig. 4. Variations of normalized conditioned vortex stretching terms $\tau_f^3\langle T_1|\xi\rangle$ (black solid lines), dilatation terms $\tau_f^3\langle T_2|\xi\rangle$ (blue dashed lines), and baroclinic torque terms $\tau_f^3\langle T_3|\xi\rangle$ (red dotted-dashed lines) sampled from (*a*) $0.09<\bar{c}_F(x,t)<0.11$ and (*b*) $0.49<\bar{c}_F(x,t)<0.51$. (For interpretation of the references to color in this figure legend, the reader is referred to the web version of this article.)

is the viscous stress tensor, δ_{kl} and ε_{ijk} designate Kronecker delta and cyclic permutation tensor, respectively. In a typical constant-density turbulent flow, the vortex-stretching term T_1 describes vorticity generation and is counter-balanced by the viscous dissipation term T_4 [50], whereas the dilatation term T_2 and the baroclinic torque term T_3 vanish. On the contrary, the dilatation term T_2 and the baroclinic torque term T_3 are known to dominate on the r.h.s. of Eq. (3) in weakly turbulent flames, with the former (latter) term reducing (increasing, respectively) enstrophy [51,52]. At very high Ka, the vortex-stretching term T_1 results statistically in increasing ω^2, overwhelms T_2 and T_3, but is counter-balanced by the viscous term T_4 [48,49], which results statistically in decreasing ω^2. Since the focus of the following discussion is placed on vorticity generation, the viscous term T_4 will not be analyzed in the rest of the paper.

The following trend shown in Fig. 4 is of the most importance for understanding the results emphasized in Figs. 1 and 2: the baroclinic torque term $\langle T_3|\xi\rangle$ is negative at $\bar{c}_F=0.1$ and $c_F(\mathbf{x},t)<0.3$, see curve plotted in red dotted-dashed line in Fig. 4a. Such a trend is much less pronounced in the middle of the flame brush, see Fig. 4b. Therefore, in the leading flame zones and in the vicinity of the flame-brush leading edge, the two terms on the r.h.s. of Eq. (3) that vanish in the case of a constant density and, hence, are controlled by combustion-induced thermal expansion, i.e., the dilatation and baroclinic torque terms T_2 and T_3, respectively, work jointly to suppress the incoming vorticity. However, while the former term works simply to reduce the vorticity magnitude, baroclinic torque not only decreases the incoming vorticity magnitude, but also generates vorticity in another tangential (to flame surface) direction (the normal component of $\nabla\rho\times\nabla p$ vanishes, because the vectors $\nabla\rho/|\nabla\rho|$ and $\mathbf{n}$ are almost collinear).

This difference in the influence of dilatation and baroclinic torque on the incoming vorticity is shown by the following vorticity transport

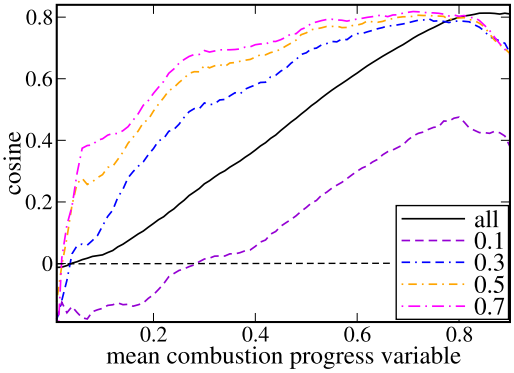

Fig. 5. Dependencies of the conditioned cosine $\langle \boldsymbol{\omega} \cdot (\nabla\rho \times \nabla p)/(|\boldsymbol{\omega}|\,|\nabla\rho \times \nabla p|)|\xi\rangle$ of an angle between vorticity and baroclinic torque vectors on c_i^* with the conditioning variable ξ being specified in legends. Black solid line shows unconditioned results.

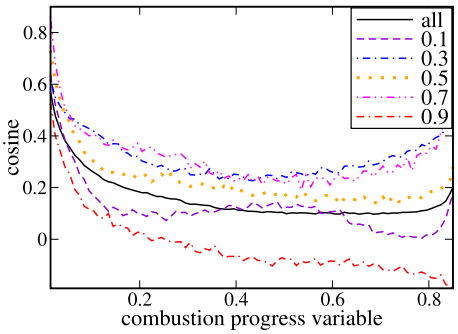

Fig. 6. Conditioned cosines $\langle \cos\gamma|\xi\rangle$ of the angle γ between tangential components of the local vorticity vector $\boldsymbol{\omega}(x_2, y, z, t)$ and the vorticity vector $\boldsymbol{\omega}(x_1, y, z, t)$ evaluated in the most left upstream point characterized by $c_F(x, y, z, t) > 0.01$. Data are sampled from different bands of $c_i^* - 0.01 < \bar{c}_F(x, t) < c_i^* + 0.01$, with c_i^* being specified in legends.

equation [7,17,49]

$$\frac{\partial \omega_i}{\partial t} + u_k \frac{\partial \omega_i}{\partial x_k} = \underbrace{\omega_k \frac{\partial u_i}{\partial x_k}}_{\mathbf{T}_1} \underbrace{-\omega_i \frac{\partial u_k}{\partial x_k}}_{\mathbf{T}_2} + \underbrace{\frac{1}{\rho^2}\varepsilon_{ijk}\frac{\partial \rho}{\partial x_j}\frac{\partial p}{\partial x_k}}_{\mathbf{T}_3} + \underbrace{\varepsilon_{ijk}\frac{\partial}{\partial x_j}\left(\frac{1}{\rho}\frac{\partial \tau_{kl}}{\partial x_l}\right)}_{\mathbf{T}_4}. \quad (4)$$

While the dilatation term $\mathbf{T}_2$ is proportional to $\boldsymbol{\omega}$, directions of vorticity and baroclinic torque vectors are different in a general case. If cosine $\cos\alpha = \boldsymbol{\omega} \cdot (\nabla\rho \times \nabla p)/(|\boldsymbol{\omega}|\,|\nabla\rho \times \nabla p|)$ of the angle α between the two vectors is negative, as happens at low $c_F(\mathbf{x}, t)$ and low $\bar{c}_F(x, t)$, see Fig. 5, baroclinic torque not only suppresses the incoming vorticity, but also generates vorticity in the tangential direction $\mathbf{t}_2$ that is perpendicular to the direction $\mathbf{t}_1$ of the incoming tangential vorticity. Since the magnitude of the negative $\langle \cos\alpha|\xi\rangle$ is significantly less than unity, see Fig. 5, projection of $\nabla\rho\times\nabla p$ on $\mathbf{t}_2$ is statistically larger than its projection on $\mathbf{t}_1$, i.e., the latter effect (vorticity generation) is stronger, but can still weakly affect enstrophy evolution, because the corresponding sub-term in T_3 in Eq. (3) involves a small $\omega_{t,2}$. Besides, unless $\omega_{t,2}$ is large, the influence of dilatation on this vorticity is weak, because dilatation term in the $\mathbf{t}_2$-component of Eq. (4) is multiplied with $\omega_{t,2}$.

Thus, at low $c_F(\mathbf{x}, t)$ and low $\bar{c}_F(x, t)$, (i) dilatation and baroclinic torque work jointly to suppress the incoming vorticity, (ii) baroclinic torque generates vorticity in another tangential (to the local flame) direction, and (iii) this effect is weakly damped by dilatation unless the magnitude $\omega_{t,2}$ of the generated vorticity reaches a sufficiently high value. As a result of such effects, the incoming vorticity is rotated in the leading flame zones, i.e., at low $c_F(\mathbf{x}, t)$.

It is worth stressing, however, that these effects neither reduce enstrophy, nor damp turbulence in the largest part of the studied flame brush. Indeed, comparison of results plotted in different lines in Fig. 3 indicates that enstrophy is increased by $\bar{c}_F$ if the mean $\bar{c}_F(x, t) \le 0.7$ and the local $c_F(\mathbf{x}, t) > 0.2$. Moreover, Fig. 4b shows that baroclinic torque dominates dilatation if $\bar{c}_F(x, t) \approx 0.5$ and $c_F(\mathbf{x}, t) > 0.3$. Thus, the effects (i)-(iii) emphasized earlier cause rotation of vorticity vector, rather than reduce ω^2.

This rotation of vorticity vector is illustrated in Fig. 6, which shows variations of the conditioned cosine $\langle \cos\gamma|\xi\rangle$ of the angle γ between (i) local and (ii) incoming tangential components of vorticity vector. This cosine is calculated for vectors $\boldsymbol{\omega}_t = \boldsymbol{\omega} - (\boldsymbol{\omega} \cdot \mathbf{n})\mathbf{n}$ taken in two points; (i) the local point, where $c_F(x_2, y, z, t) \approx \xi$, and (ii) an upstream point, where $c_F(x_1, y, z, t) \approx 0.01$. To avoid interpolation, these data were solely sampled from lines almost parallel to x-axis, i.e., from horizontal lines that contain at least one point where $|n_x| > 0.95$ provided that $0.3 < c_F(\mathbf{x}, t) < 0.7$ (the reported trends are weakly sensitive to the threshold value of $|n_x|$ provided that it is larger than 0.9). A rapid decrease in $\langle \cos\gamma|\xi\rangle$ with increasing ξ is clearly observed at $\xi < 0.2$ (data sampled at $\xi < 0.05$ are highly scattered and not shown). As a result, $\langle \cos\gamma|\xi\rangle < 0.4$ if $\xi > 0.2$, i.e., the vectors $\boldsymbol{\omega}_t(x_1, y, z, t)$ and $\boldsymbol{\omega}_t(x_2, y, z, t)$ have (statistically) almost perpendicular directions.

At larger $c_F(\mathbf{x}, t)$ and $\bar{c}_F(x, t)$, cosine of an angle between $\boldsymbol{\omega}$ and $\nabla\rho \times \nabla p$ becomes positive, see Fig. 5, and enstrophy is increased by baroclinic torque. Indeed, (i) $\langle |T_2||\xi\rangle$ is positive and significantly larger than $\langle |T_2||\xi\rangle$ in the middle of the flame brush, cf. curves plotted in red dotted-dashed and blue dashed lines in Fig. 4b, and, accordingly, (ii) $\langle \omega^2|\xi\rangle$ increases with increasing $\bar{c}_F(x, t)$ if $\bar{c}_F(x, t) < 0.8$ and $c_F(\mathbf{x}, t) > 0.3$, see Fig. 3. Thus, baroclinic torque not only damps incoming vorticity in the leading flame zones, but also generates vorticity in another tangential direction, with this rotation of vorticity vector contributing to flame-generated turbulence at larger $c_F(\mathbf{x}, t)$. However, as directions of the incoming vorticity and vorticity generated by baroclinic torque are different, see Fig. 6, solenoidal velocity fluctuations associated with the latter vorticity can work to statistically smooth flame-surface perturbations, as happens under conditions of the present study, see Figs. 1 and 2. The point is that the flame surface is created not only by solenoidal velocity fluctuations, but also and mainly by potential velocity fluctuations generated by combustion-induced pressure perturbations, with the mean strain rate created by the potential velocity fluctuations being positive and large, see Fig. 2. It is not known *a priori* whether effects of such a potential turbulence and solenoidal turbulence generated by baroclinic torque at large $c_F(\mathbf{x}, t)$ on flame surface perturbations are similar or opposite. The above analysis shows that the two effects are opposite under conditions of the present study, see Fig. 2. This situation is not unique, with the same phenomenon being predicted by the theory of hydrodynamic instability of an infinitely thin laminar flame sheet [5]. According to the theory, wrinkles of a laminar flame sheet grow under the influence of potential flow perturbations, whereas solenoidal velocity perturbations generated behind the sheet work to mitigate the wrinkle growth [5–7]. Nevertheless, further research into the influence of combustion-generated vorticity on flame surface area is required at various Ka, for different flame configurations, e.g., jet flames [42,43,45], etc.

Finally, it is worth noting that vorticity rotation in premixed turbulent flames, explored in the present work, has some common features with the phenomenon of vorticity tilting and vortex re-connection [53, 54], documented experimentally by Holzner et al. [55] in homogeneous constant-density turbulence, or rotation of strain-rate eigenframe in premixed flames, investigated by Zhao et al. [56] in their DNS study of weakly turbulent combustion.

4. Concluding remarks

Complex-chemistry DNS data obtained earlier from a moderately lean hydrogen-air turbulent flame were analyzed adopting several dif-

ferent numerical diagnostic techniques, with results yielded by all these techniques indicating consistent trends, thus, validating the performed analysis. Specifically, the analysis shows that the rotational motion acts to smooth wrinkles of iso-scalar surfaces within local preheat and reaction zones and, consequently, to reduce flame surface area. This physical mechanism arises because baroclinic torque works to suppress the incoming tangential (to the flame) vorticity, but to generate vorticity in another tangential direction. Under conditions of the present study, solenoidal velocity fluctuations associated with the latter (flame-generated) vorticity work statistically to smooth flame surface and flame surface area is primarily created by potential velocity perturbations caused by combustion-induced thermal expansion. Such effects play an important role even in sufficiently intense small-scale turbulence considered in this work (a ratio of laminar flame thickness to Kolmogorov length scale is about 20 and $Ka > 1$).

The present results, earlier DNS data [14,15] obtained from weakly turbulent single-step-chemistry flames, and experimental data by Steinberg et al. [13] challenge the classical concept of combustion acceleration due to flame-generated turbulence [57], at least if turbulence is associated with rotational motion. When compared to the earlier aforementioned data [13–15], the present results were obtained from sufficiently intense, small-scale turbulence characterized by Damköhler and Karlovitz numbers on the order on and larger than unity, respectively. As far as highly turbulent flames are concerned, the influence of combustion-induced thermal expansion on vorticity field is expected to vanish at $Da \ll 1$ and $Ka \gg 1$ [48,49], see also recent review articles [16,17].

Novelty and significance statement

The novelty of research consists in demonstrating that, even in intense, small-scale turbulence, flame surface area is mainly created by potential velocity fluctuations generated due to thermal expansion, whereas solenoidal velocity fluctuations work statistically to reduce the area. These findings are significant, because they challenge the classical concept of flame-generated turbulence and show that turbulence faced by a flame differs fundamentally from constant-density rotational motion.

CRediT authorship contribution statement

Andrei N. Lipatnikov: Analyzed DNS data, Created figures, Wrote the paper. **Vladimir A. Sabelnikov:** Analyzed computed results, Edited the paper. **Nikolay V. Nikitin:** Developed software for Helmholtz–Hodge decomposition, Edited the paper.

Declaration of competing interest

The authors declare that they have no known competing financial interests or personal relationships that could have appeared to influence the work reported in this paper.

Acknowledgments

The authors are very grateful to Prof. Chaudhuri and Dr. Dave for sharing their DNS data with us. A.N.L. acknowledges the financial support by Swedish Research Council (Grant No. 2023-04407) and Chalmers Area of Advance “Transport” (Grant No. 2021-0040). V.A.S. gratefully acknowledges the financial support by ONERA, France and the Ministry of Science and Higher Education of the Russian Federation (Grant Agreement of December 8, 2020, No. 075-11-2020-023).

References

[1] P.-H. Renard, D. Thévenin, J.C. Rolon, S. Candel, Dynamics of flame/vortex interactions, Prog. Energy Combust. Sci. 26 (2000) 225–282.
[2] F. Thiesset, G. Maurice, F. Halter, N. Mazellier, C. Chauveau, I. Gökalp, Flame-vortex interaction: Effect of residence time and formulation of a new efficiency function, Proc. Combust. Inst. 36 (2017) 1843–1851.
[3] P.L.K. Paes, Y.G. Shah, J.G. Brasseura, Y. Xuan, A scaling analysis for the evolution of small-scale turbulence eddies across premixed flames with implications on distributed combustion, Combust. Theory Modell. 24 (2020) 307–325.
[4] S. Luna, F.N. Egolfopoulos, Local effects in vortex-flame interactions: Implications for turbulent premixed flame scaling and observables, Combust. Flame 245 (2022) 112293.
[5] L.D. Landau, E.M. Lifshitz, Fluid Mechanics, Pergamon Press, New York, 1987.
[6] Ya.B. Zel’dovich, G.I. Barenblatt, V.B. Librovich, G.M. Makhviladze, The Mathematical Theory of Combustion and Explosions, Plenum, New York, 1985.
[7] A.N. Lipatnikov, J. Chomiak, Effects of premixed flames on turbulence and turbulent scalar transport, Prog. Energy Combust. Sci. 36 (2010) 1–102.
[8] C.J. Mueller, J.F. Driscoll, D.L. Reuss, M.C. Drake, M.E. Rosalik, Vorticity generation and attenuation as vortices convect through a premixed flame, Combust. Flame 112 (1998) 342–346.
[9] J.O. Sinibaldi, C.J. Mueller, A.E. Tulkki, J.F. Driscoll, Suppression of flame wrinkling by buoyancy: The baroclinic stabilization mechanism, AIAA J. 36 (1998) 1432–1438.
[10] D. Louch, K.N.C. Bray, Vorticity and scalar transport in premixed turbulent combustion, Proc. Combust. Inst. 27 (1998) 801–810.
[11] D. Louch, K.N.C. Bray, Vorticity in unsteady premixed flames: Vortex pair-premixed flame interactions under imposed body forces and various degrees of heat release and laminar flame thickness, Combust. Flame 125 (2001) 1279–1309.
[12] K.L. Pan, J. Qian, C.K. Law, W. Shyy, The role of hydrodynamic instability in flame–vortex interaction, Proc. Combust. Inst. 29 (2002) 1695–1704.
[13] A.M. Steinberg, J.F. Driscoll, S.L. Ceccio, Measurements of turbulent premixed flame dynamics using cinema stereoscopic PIV, Exp. Fluids 44 (2008) 985–999.
[14] A.N. Lipatnikov, V.A. Sabelnikov, S. Nishiki, T. Hasegawa, Does flame-generated vorticity increase turbulent burning velocity? Phys, Fluids 30 (2018) 081702.
[15] A.N. Lipatnikov, V.A. Sabelnikov, S. Nishiki, T. Hasegawa, A direct numerical simulation study of the influence of flame-generated vorticity on reaction-zone-surface area in weakly turbulent premixed combustion, Phys. Fluids 31 (2019) 055101.
[16] V.A. Sabelnikov, A.N. Lipatnikov, Recent advances in understanding of thermal expansion effects in premixed turbulent flames, Annu. Rev. Fluid Mech. 49 (2017) 91–117.
[17] A.M. Steinberg, P.E. Hamlington, X. Zhao, Structure and dynamics of highly turbulent premixed combustion, Prog. Energy Combust. Sci. 85 (2021) 100900.
[18] H.L. Dave, A. Mohan, S. Chaudhuri, Genesis and evolution of premixed flames in turbulence, Combust. Flame 196 (2018) 386–399.
[19] H.L. Dave, S. Chaudhuri, Evolution of local flame displacement speeds in turbulence, J. Fluid Mech. 884 (2020) A46.
[20] A.N. Lipatnikov, V.A. Sabelnikov, An extended flamelet-based presumed probability density function for predicting mean concentrations of various species in premixed turbulent flames, Int. J. Hydrogen Energy 45 (2020) 31162–31178.
[21] A.N. Lipatnikov, V.A. Sabelnikov, Evaluation of mean species mass fractions in premixed turbulent flames: A DNS study, Proc. Combust. Inst. 38 (2021) 6413–6420.
[22] A.N. Lipatnikov, V.A. Sabelnikov, Flame folding and conditioned concentration profiles in moderately intense turbulence, Phys. Fluids 34 (2022) 065119.
[23] V.A. Sabelnikov, A.N. Lipatnikov, S. Nishiki, H.L. Dave, F.L. Hernández Pérez, W. Song, H.G. Im, Dissipation and dilatation rates in premixed turbulent flames, Phys. Fluids 33 (2021) 035112.
[24] A.N. Lipatnikov, A priori test of perfectly stirred reactor approach to evaluating mean fuel consumption and heat release rates in highly turbulent premixed flames, Int. J. Engine Res. 24 (2023) 4034–4043.
[25] A.N. Lipatnikov, V.A. Sabelnikov, Influence of small-scale turbulence on internal flamelet structure, Phys. Fluids 35 (2023) 055128.
[26] J. Li, Z. Zhao, A. Kazakov, F.L. Dryer, An updated comprehensive kinetic model of hydrogen combustion, Int. J. Chem. Kinetics 36 (2004) 566–575.
[27] A.N. Lipatnikov, V.A. Sabelnikov, Karlovitz numbers and premixed turbulent combustion regimes for complex-chemistry flames, Energies 15 (2022) 5840.
[28] A.N. Lipatnikov, J. Chomiak, Molecular transport effects on turbulent flame propagation and structure, Prog. Energy Combust. Sci. 31 (2005) 1–73.
[29] A.J. Aspden, M.S. Day, J.B. Bell, Turbulence-flame interactions in lean premixed hydrogen: Transition to the distributed burning regime, J. Fluid Mech. 680 (2011) 287320.
[30] V.A. Sabelnikov, A.N. Lipatnikov, N. Nikitin, S. Nishiki, T. Hasegawa, Solenoidal and potential velocity fields in weakly turbulent premixed flames, Proc. Combust. Inst. 38 (2021) 3087–3095.
[31] V.A. Sabelnikov, A.N. Lipatnikov, N. Nikitin, F.E. Hernández-Pérez, H. Im, Conditioned structure functions in turbulent hydrogen/air flames, Phys. Fluids 34 (2022) 085103.
[32] V.A. Sabelnikov, A.N. Lipatnikov, N. Nikitin, F.E. Hernández-Pérez, H. Im, Effects of thermal expansion on moderately intense turbulence in premixed flames, Phys. Fluids 34 (2022) 115127.
[33] V.A. Sabelnikov, A.N. Lipatnikov, N. Nikitin, F.E. Hernández-Pérez, H. Im, Backscatter of scalar variance in turbulent premixed flames, J. Fluid Mech. 960 (2023) R2.

[34] A.M. Klimov, Laminar flame in a turbulent flow, Zh. Prikl. Mekch. Tekhn. Fiz. 4 (3) (1963) 49–58.
[35] J. Buckmaster, The quenching of two-dimensional premixed flames, Acta Astronaut. 6 (1979) 741–769.
[36] M. Matalon, On flame stretch, Combust. Sci. Technol. 31 (1983) 169–182.
[37] P. Clavin, Dynamical behavior of premixed flame fronts in laminar and turbulent flows, Prog. Energy Combust. Sci. 11 (1985) 1–59.
[38] S. Candel, T. Poinsot, Flame stretch and the balance equation for the flame area, Combust. Sci. Techol. 170 (1990) 1–15.
[39] S.B. Pope, The evolution of surface in turbulence, Internat. J. Engrg. Sci. 26 (1988) 445–469.
[40] D. Veynante, L. Vervisch, Turbulent combustion modeling, Prog. Energy Combust. Sci. 28 (2002) 193–266.
[41] N. Chakraborty, R.S. Cant, Effects of strain rate and curvature on surface density function transport in turbulent premixed flames in the thin reaction zones regime, Phys. Fluids 17 (2005) 065108.
[42] H. Wang, E.R. Hawkes, J.H. Chen, B. Zhou, Z. Li, M. Aldén, Direct numerical simulations of a high Karlovitz number laboratory premixed jet flame - an analysis of flame stretch and flame thickening, J. Fluid. Mech. 815 (2017) 511–536.
[43] S. Luca, A. Attili, E.L. Schiavo, F. Creta, F. Bisetti, On the statistics of flame stretch in turbulent premixed jet flames in the thin reaction zone regime at varying Reynolds number, Proc. Combust. Inst. 37 (2019) 2451–2459.
[44] E. Suillaud, K. Truffin, O. Colin, D. Veynante, Direct numerical simulations of high Karlovitz number premixed flames for the analysis and modeling of the displacement speed, Combust. Flame 236 (2022) 111770.
[45] L. Berger, A. Attili, H. Pitsch, Synergistic interactions of thermodiffusive instabilities and turbulence in lean hydrogen flames, Combust. Flame 244 (2022) 112254.
[46] H.C. Lee, P. Dai, M. Wan, A.N. Lipatnikov, Displacement speed, flame surface density, and burning rate in highly turbulent premixed flames characterized by low Lewis numbers, J. Fluid. Mech. 961 (2023) A21.
[47] Wm.T. Ashurst, A.R. Kerstein, R.M. Kerr, C.H. Gibson, Alignment of vorticity and scalar gradient with strain rate in simulated Navier–Stokes turbulence, Phys. Fluids 30 (1987) 2343–2353.
[48] P.E. Hamlington, A.Y. Poludnenko, E.S. Oran, Interactions between turbulence and flames in premixed reacting flows, Phys. Fluids 23 (2011) 125111.
[49] B. Bobbitt, S. Lapointe, G. Blanquart, Vorticity transformation in high Karlovitz number premixed flames, Phys. Fluids 28 (2016) 015101.
[50] A. Tsinober, The Essence of Turbulence as a Physical Phenomenon. With Emphasis on Issues of Paradigmatic Nature, 2nd ed., Springer Nature, Switzerland, 2019.
[51] A.N. Lipatnikov, S. Nishiki, T. Hasegawa, A direct numerical simulation study of vorticity transformation in weakly turbulent premixed flames, Phys. Fluids 26 (2014) 105104.
[52] N. Chakraborty, I. Konstantinou, A.N. Lipatnikov, Effects of Lewis number on vorticity and enstrophy transport in turbulent premixed flames, Phys. Fluids 28 (2016) 015109.
[53] H. Tennekes, J.L. Lumley, A First Course in Turbulence, MIT Press, Cambridge, MA, 1972.
[54] S. Kida, M. Takaoka, Vortex reconnection, Annu. Rev. Fluid Mech. 26 (1994) 169–189.
[55] M. Holzner, M. Guala, B. Lüthi, A. Liberzon, N. Nikitin, W. Kinzelbach, A. Tsinober, Viscous tilting and production of vorticity in homogeneous turbulence, Phys. Fluids 22 (2010) 061701.
[56] S. Zhao, A. Er-raiy, Z. Bouali, A. Mura, Dynamics and kinematics of the reactive scalar gradient in weakly turbulent premixed flames, Combust. Flame 198 (2018) 436–454.
[57] B. Karlovitz, D.W. Denniston, F.E. Wells, Investigation of turbulent flames, J. Chem. Phys. 19 (1951) 541–547.